**European Journal of Remote Sensing**
An official journal of the Italian Society of Remote Sensing

www.aitjournal.com

# 3D displacement field retrieved by integrating Sentinel-1 InSAR and GPS data: the 2014 South Napa earthquake

**Marco Polcari[1,5]\*, Mimmo Palano[2], José Fernández[3], Sergey V. Samsonov[4], Salvatore Stramondo[1] and Susanna Zerbini[5]**

[1]Istituto Nazionale di Geofisica e Vulcanologia, Via di Vigna Murata 605, 00143 Rome, Italy
[2]Istituto Nazionale di Geofisica e Vulcanologia, Osservatorio Etneo,
Piazza Roma 2, 95125 Catania, Italy
[3]Instituto de Geocencias (IGEO) (CSIC, UCM). Plaza de Ciencias 3, 28040 Madrid, Spain
[4]Canada Centre for Mapping and Earth Observation, Natural Resources Canada, 560
Rochester Street, ON K1A 0E4, Ottawa, Canada
[5]University of Bologna, Department of Physics and Astronomy,
Viale Berti Pichat 8, 40127 Bologna, Italy
\*Corresponding author, e-mail address: marco.polcari@ingv.it

## Abstract

In this study the integration of Sentinel-1 InSAR (Interferometric Synthetic Aperture Radar) and GPS (Global Positioning System) data was performed to estimate the three components of the ground deformation field due to the Mw 6.0 earthquake occurred on August 24th, 2014, in the Napa Valley, California, USA. The SAR data were acquired by the Sentinel-1 satellite on August 7th and 31st respectively. In addition, the GPS observations acquired during the whole month of August were analyzed. These data were obtained from the Bay Area Regional Deformation Network, the UNAVCO and the Crustal Dynamics Data Information System online archives. The data integration was realized by using a Bayesian statistical approach searching for the optimal estimation of the three deformation components. The experimental results show large displacements caused by the earthquake characterized by a predominantly NW-SE strike-slip fault mechanism.
**Keywords:** SAR interferometry, GPS, Sentinel-1, Earthquake, 3D displacement.

## Introduction

The possibility of merging data provided by different geodetic techniques to retrieve the three dimensional (3D) components of a surface displacement field is widely debated in literature [Gudmunsson and Sigmundsson, 2002; Samsonov et al., 2007; González et al., 2010; Guglielmino et al., 2011] and is still one of the most exciting challenges for the scientific "geodetic and remote sensing" community. Today, InSAR and GPS are two of the most important sources of information concerning the Earth's topography and surface deformation that can be synergistically combined with LiDAR and optical data [Joyce et al., 2014].

Moreover, InSAR and GPS data are fully complementary and suitable to be integrated in order to estimate an accurate 3D displacement field, with millimeter precision and large spatial coverage.

Indeed, InSAR data allow covering areas of hundreds of square kilometers with a spatial resolution ranging from a few meters to > 20 m depending on the satellite and the acquisition mode.

In particular, InSAR measures the range distance between the Earth's surface and the sensor along the satellite Line-of-Sight (LOS). Since the satellites usually acquire data with an incidence angle spanning about 20°-30°, the measured LOS displacement is particularly sensitive to the vertical displacement. Therefore, due to the viewing geometry, InSAR can better constrain deformation fields mainly characterized by a vertical component as is the case of subsidence [Stramondo et al., 2008; Polcari et al., 2014] or volcanos inflation/deflation [Palano et al., 2008; Malinverni et al., 2014; Fernández et al., 2015; Trasatti et al., 2015].

On the other hand, a permanent GPS station provides the estimation of absolute and continuous 3D site coordinates. Then, the key contribution with respect to the InSAR data is the time-continuous information. The main drawback is the relatively low spatial density of the GPS networks. Typically, the distance between stations belonging to the same network ranges from a few to tens of kilometers according to the wavelength of the signal to be monitored. Therefore, the information provided by GPS needs oftentimes to be interpolated; this process might lead to errors proportional to the distance among stations so that the entire signal is missing if it falls completely between stations.

The present study proposes an InSAR-GPS data integration [Samsonov and Tiampo, 2006] using Sentinel-1 SAR data acquired at the time of occurrence (August 24th, 2014) of the Mw 6.0 South Napa earthquake. The epicenter of this earthquake was located within the western sector of the West Napa Fault system, a strike-slip crustal structure between the Rodger's Creek and Green Valley faults, with nearly pure NNW attitude [Barnhart et al., 2015].

Sentinel-1A was launched on April 3rd 2014, from the European Spaceport in French Guiana, representing the first of a constellation of two satellites (Sentinel-1A and Sentinel-1B). It carries an advanced C-band polar-orbiting radar providing all-weather and day-and-night images of Earth's surface. The revisit time is significantly improved with respect to those of the ERS 1-2 and Envisat satellites (6-12 vs 35-70 days).

In addition, the more common acquisition mode is the Interferometric Wide swath (IW) implementing a new type of ScanSAR called Terrain Observation with Progressive Scan (TOPS), which allows significantly extending the ground coverage with a 250 km swath at about 5 m range by 20 m azimuth spatial resolution.

The system is also able to acquire data in Stripmap mode and in Extra Wide (EW) swath mode allowing to improve the pixel resolution or the areal coverage, according to the scale of the studied phenomenon and the details required by the specific application.

All these improvements make Sentinel-1 an innovative tool for the Earth's surface observation. Therefore, the integration with increasingly dense GPS networks will play a key role in the study of natural phenomena at different spatial and temporal scales (e.g., faults motion, volcanic inflation/deflation, landmass subsidence, etc.).

## InSAR-GPS integration: theory

The method used for integrating InSAR and GPS data was originally proposed by Samsonov et al. [2006], and is based on a Bayesian statistical approach searching for the optimal estimation of the three deformation rate components.

The InSAR deformation rate estimated along the satellite LOS can be expressed as follows:

$$V_{LOS}^{i} = \left[ v_x^i, v_y^i, v_z^i \right] \left[ -\cos a \sin\theta, \sin\alpha \sin\theta, \cos\theta \right]^T \quad [1]$$

where $V_{LOS}^{i}$ is the InSAR LOS deformation rate defined on a grid of N points, $\left[ v_x^i, v_y^i, v_z^i \right]$ are the east, north and vertical unknown components of the deformation rate, and $\theta$ and $\alpha$ are the incidence and the azimuth angle of the satellite, respectively.

The GPS velocities are:

$$\left[ V_x^i, V_y^i, V_z^i \right] \quad [2]$$

Since the velocities from [2] can be estimated only at sparse locations corresponding to the available GPS sites, it is necessary to adopt an interpolation approach. In particular, in order to merge InSAR and GPS data, the GPS velocities need to be interpolated and resampled onto the InSAR grid points. To do so, the Kriging interpolation method is applied [Brooker, 1991], while the most probable deformation rate components are searched by using the Bayes inference theory. The Bayes theory is widely used in decision-making problems allowing the estimation of an unknown parameter or a random variable by observing another random variable and knowing the joint probability density distribution.

In particular, let $\alpha$ be an unknown parameter to be estimated and $b$ the N observations of the random variable $B$.

In the Bayes estimation, the best performance (optimal estimation) is obtained when the estimate $\hat{\alpha}$ of the unknown parameter $\alpha$ is such to minimize the Bayes risk.

The Bayes risk of $\hat{\alpha}$ can be expressed as follows [Li, 2001]:

$$R\left(\hat{\alpha}\right) = \int_{a \in A} C\left(a, \hat{\alpha}\right) P\left(a \, / \, b\right) da \quad [3]$$

where A is the space of the parameters, $P\left(a \, / \, b\right)$ is the *a posteriori* distribution and $C\left(a, \hat{\alpha}\right)$ is a cost function defined as:

$$C\left(a, \hat{a}\right) = \begin{cases} 0 \; if \; \left\| \hat{a} - a \right\| \leq \delta \\ 1 \; otherwise \end{cases} \quad [4]$$

where $\boldsymbol{\delta}$ is any small constant.

Then, Equation [3] becomes:

$$R\left(\hat{a}\right) = \int_{a:\|\hat{a}-a\|>\delta} P\left(a/b\right)da = 1 - \int_{a:\|\hat{a}-a\|\leq\delta} P\left(a/b\right)da \quad [5]$$

As $\delta \to 0$ the Bayes risk of the estimate can be rewritten as:

$$R\left(\hat{a}\right) \cong 1 - P\left(a/b\right) \quad [6]$$

Therefore, minimizing the Bayes risk is equivalent to maximizing the *a posteriori* distribution that can be calculated by exploiting the Bayes theorem:

$$P\left(a/b\right) = \frac{P\left(b/a\right)P\left(a\right)}{P\left(b\right)} \propto P\left(b/a\right) \quad [7]$$

where $P(b/a)$ is the likelihood of the observation b, $P(a)$ is the *a priori* density distribution and $P(b)$ is the density of b that can be ignored since b is given.

In addition, in many application fields such as the image analysis, the *a priori* density distribution, $P(a)$, is not used, being related to the reliability of the model developed for the estimation. Then, it will be neglected in the subsequent computations.

With these assumptions, the $\hat{\alpha}$ value minimizing the risk is the same as maximizing the likelihood, thus leading to the Maximum Likelihood Estimation (MLE).

As explained in details by Li [2001], the likelihood can be estimated according to the Hammersley-Clifford theorem stating that any conditional distribution, under some conditions, has a distribution which is represented by a Gibbs function:

$$P\left(b/a\right) = \frac{1}{\prod_{i=1}^{N}\sqrt{2\pi\sigma_i^2}}\,e^{-U(b/a)} \quad [8]$$

where $U(b/a)$ is the likelihood energy, defined as:

$$U\left(b/a\right) = \sum_{i=1}^{N}\frac{\left(b_i-a_i\right)^2}{2\sigma_i^2} \quad [9]$$

Here, a Gaussian noise was assumed since it is a special member of the Gibbs distribution family. Equation [8] states that the likelihood is proportional to the function $e^{-U(b/a)}$, then the MLE of a, i.e. $\hat{\alpha}$, is obtained in equivalent manner by minimizing the likelihood energy function in [9].

Therefore, the *a posteriori* distribution [7] can be expressed in terms of energy functions as follows:

$$U\left(a/b\right) \propto U\left(b/a\right) = \sum\nolimits_{i=1}^{N} \frac{\left(b_i - a_i\right)^2}{2\sigma_i^2} \quad [10]$$

Finally, by applying [10] to the case of the InSAR-GPS measurements is possible to retrieve the MLE estimate of the three optimized deformation rate components:

$$U\left(v_x, v_y, v_z / V_{LOS}, V_x, V_y, V_z\right) = \sum\nolimits_{i=1}^{N} \frac{1}{\left(2\sigma_{sar}^i\right)^2} \left(V_{LOS}^i + v_x \cos(a)\cos(\theta) - v_y \sin(a) - v_z \cos(\theta)\right)^2 +$$

$$\frac{1}{\left(2\sigma_{x_{gps}}^i\right)^2}\left(V_x^i - v_x^i\right)^2 + \frac{1}{\left(2\sigma_{y_{gps}}^i\right)^2}\left(V_y^i - v_y^i\right)^2 + \frac{1}{\left(2\sigma_{z_{gps}}^i\right)^2}\left(V_z^i - v_z^i\right)^2 \quad [11]$$

where:
- $N$ is the number of points of the InSAR and interpolated-GPS grid images;
- $v_x$, $v_y$, $v_z$ are the three unknown components of the deformation rate, i.e. the unknown parameters in [10];
- $V_{LOS}$, $V_x$, $V_y$, $V_z$ are the observations from InSAR and GPS respectively, i.e., the known parameters $b_i$ in [10];
- $\dfrac{1}{2\sigma_{sar}^2}, \dfrac{1}{2\sigma_{x_{gps}}^2}, \dfrac{1}{2\sigma_{y_{gps}}^2}, \dfrac{1}{2\sigma_{z_{gps}}^2}$ are the standard deviations of the InSAR and GPS measurements, respectively.

Therefore, the three components of the deformation rate for each point of the image are found by minimizing Equation [11].

## Geodetic data
### InSAR data
The SAR data provided by Sentinel-1 were acquired in Stripmap mode with an incidence angle of 23° and a pixel resolution of 4 meters in both directions covering an area of about 70x180 Km². A single pair of SAR images was exploited in order to detect and measure the co-seismic displacement caused by the earthquake. The pre- and post-earthquake images were acquired on August 7th 2014 and on August 31st 2014, respectively. The resulting image pair, characterized by a perpendicular baseline of 2 meters, was processed using the GAMMA software [Wegmuller and Werner, 1997].
In order to focus on the epicentral area, the data have been cut and multi-looked by a factor of 15 in both range and azimuth to obtain a 60x60m pixel posting. The SRTM Digital Elevation Model (DEM) has been used to remove the topographic phase. Moreover, the Minimum Cost Flow (MCF) algorithm [Costantini, 1998] has been applied for phase unwrapping following a phase filtering [Goldstein and Werner, 1998]. As portrayed in Figure 1, the resulting differential interferogram shows interferometric fringes allowing the detection of a significant surface displacement caused by the earthquake.
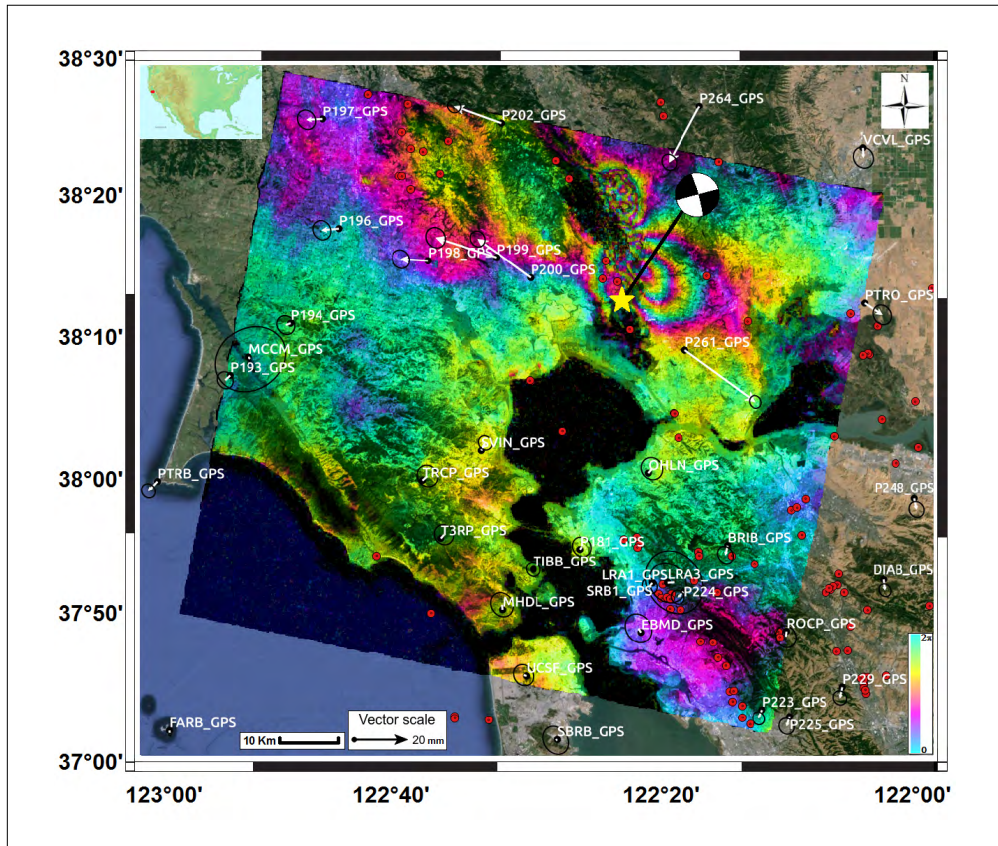
**Figure 1 - Wrapped interferogram showing co-seismic LOS displacement (each fringe corresponds to 2.8 cm). GPS sites with co-seismic displacement vectors are shown in white. GPS co-seismic displacement was estimated by differencing the average site positions over 2 days before and after the event. Yellow star indicate the Mw 6.0 epicenter location. Mw>3.5 seismicity (red circles) and focal mechanism related to the Mw 6.0 earthquake are also reported (http://earthquake.usgs.gov/ earthquakes).**

### GPS data

The analyzed GPS dataset, covering the time interval August 1st 2014 - September 2nd 2014, includes 27 stations belonging to the Bay Area Regional Deformation Network (BARDN) and 115 additional continuous stations whose data are available in the UNAVCO and in the Crustal Dynamics Data Information System (CDDIS) archives. The GNNS raw observations were processed by means of the GAMIT/GLOBK 10.5 software (http://www-gpsg.mit. edu), using precise IGS orbits (International GNSS Service; http://igscb.jpl.nasa.gov) and the IERS Earth orientation parameters (International Earth Rotation Service; http://www. iers.org). All stations have been organized and processed into three sub-networks, each one including about 50 stations and sharing a few common sites to provide the necessary ties between them. The results of this processing step are daily estimates of loosely constrained station coordinates, along with the associated variance-covariance matrices. In a successive step, these loosely constrained daily solutions were used as quasi observations in a Kalman

filtering (GLOBK) in order to estimate a consistent set of daily coordinates (i.e. time series) for all the sites involved. The resulting time series were aligned to a North America fixed reference frame [Altamimi et al., 2012]. A simple visual inspection of the coordinates time series of the stations located close to the epicentral area allowed to detect a significant offset ascribed to the co-seismic deformation (Fig. 3).

## Results

Since the aim of this study is to evaluate the co-seismic surface deformation caused by the Napa Valley earthquake, the results are provided in terms of optimized displacement field components instead of deformation rate. Hence, by applying the approach described above and using as input the co-seismic InSAR map and the GPS measurements, the 3D components of the surface displacement field have been estimated.

The experimental results show a strong N-S component of the displacement field (Fig. 2A), clearly indicating a strike-slip fault mechanism, with an approximately right lateral displacement along a NW-SE trending fault plane, according to the estimated focal mechanism (Fig. 1), and ~340°/165° strike depending on the dip (east-dipping or west-dipping, respectively). This is also in agreement with previous works showing a rupture propagating NNW for about 15 Km [Barnhart et al., 2015] and reaching the surface with a maximum slip of about 46 cm near the city of Napa [Hudnut et al., 2014]. Also he E-W component is significant, especially along the southern part of the fault (Fig. 2B). Indeed, as pointed out in previous studies [Hudnut et al., 2014; Wei et al., 2015], the fault strike rotates by about 15° counterclockwise from N to S along the rupture, near the sites where slip peaks.

In addition, it is worth noting a small, but not negligible, vertical displacement detected in the north-east side of the fault, where a subsidence of about 8 cm occurred (Fig. 2C). Such a behavior can also be observed in the time series of the two GPS stations closely located to the epicentre (see Fig. 3), on the right (P261) and left (P200) side of the seismogenic fault, respectively (Fig. 2C). The co-seismic jump is well noticeable in the time series of both stations, which show significant displacements along the N-S and the E-W components on August 24th, 2014.

Particular care is required to explain the results at the NE side of the fault plane. Indeed, this area shows a minor S-ward motion with respect to the SE side (Fig. 2A), but it is also characterized by significant subsidence (Fig. 2C). The lack of GPS stations results in a deformation mainly derived from the InSAR data that are not fully suitable in constraining the N-S component due to the orbital configuration. However, the deformation gradient is located close to the city of Napa, where field investigations by Hudnut et al. [2014] revealed a strike rotation that might have led to the estimated pattern.

Table 1 provides an evaluation of the performance of the adopted method. In particular, the standard deviation for a point close to the epicenter is shown. As expected, the north component does not show any major change since the InSAR data are less sensitive to the motion along that component. On the other hand, a significant improvement of the east and up components by the optimization step is clearly noticeable.
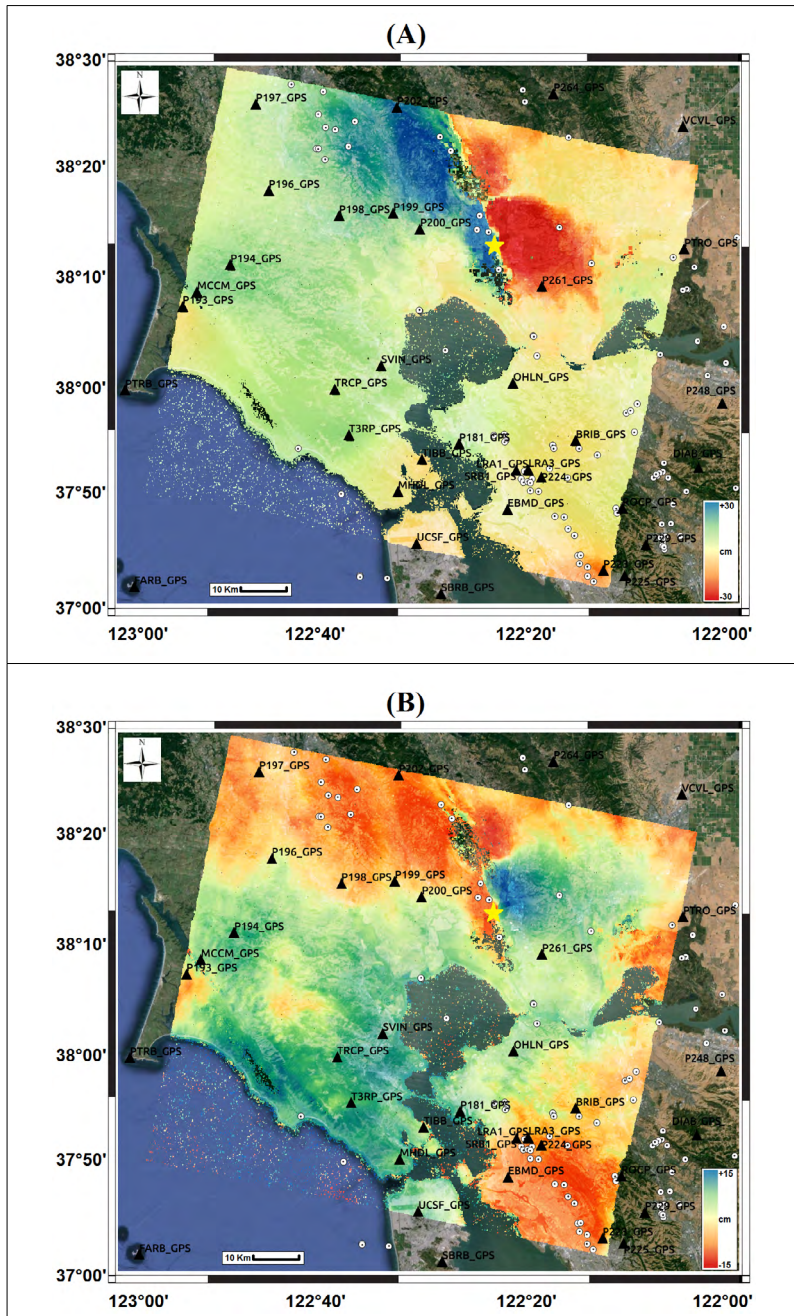
**Figure 2 (Continued on next page) - 3D optimized components of surface displacement field caused by the earthquake. N-S component (A), E-W component (B) and U-D component (C). GPS sites are indicated with the black triangles. Star indicates the Mw 6.0 epicenter location. Mw>3.5 seismicity is also shown (http://earthquake.usgs.gov/earthquakes).**
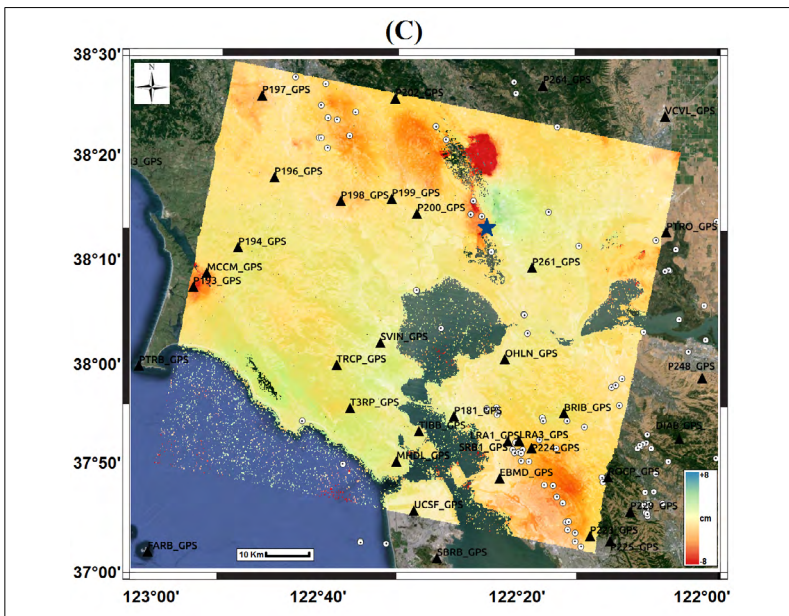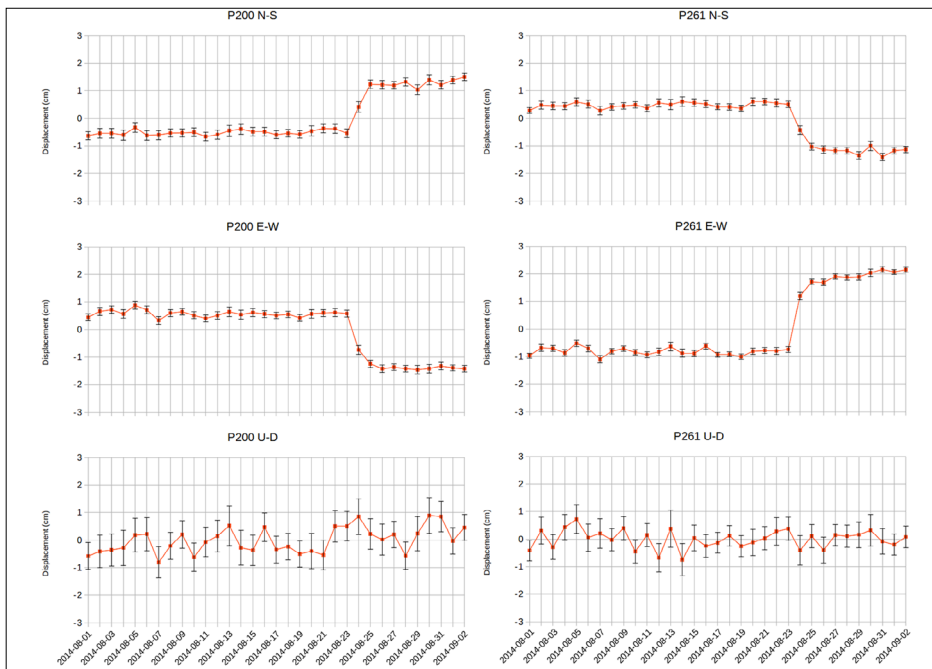
**Figure 2 (Continued from preceding page) - 3D optimized components of surface displacement field caused by the earthquake. N-S component (A), E-W component (B) and U-D component (C). GPS sites are indicated with the black triangles. Star indicates the Mw 6.0 epicenter location. Mw>3.5 seismicity is also shown (http://earthquake.usgs.gov/earthquakes).**



**Figure 3 - Time series of North-South (upper panel), East-West (central panel) and Up-Down (bottom panel) displacements of stations P200 (left side) and P261 (right side).**

Table 1 - σ (cm) of north, east and up components estimated before and after the optimization step for a point close the epicenter. Here GPS data are meant as the interpolated GPS data.

|            | $\sigma_{NS}$ | $\sigma_{EW}$ | $\sigma_{UD}$ |
|------------|---------------|---------------|---------------|
| **GPS**    | 0.538         | 0.514         | 1.097         |
| **InSAR+GPS** | 0.531      | 0.427         | 0.596         |

## Discussion and conclusions

In this work, the performance of the InSAR-GPS data integration technique, developed by Samsonov et al. [2006], has been assessed by using Sentinel-1 InSAR data and the GPS observations of the BARDN and those of 115 additional stations to retrieve the 3D displacement map induced by the 2014 Napa Valley earthquake.

The co-seismic slip reached the surface, producing a 15 km-long rupture extending through vineyards, roads and even houses causing significant damages and about 200 injured [Hudnut et al., 2014].

The InSAR-GPS integration method works quite well revealing 3D components of the surface deformation field compatible with the fault geometry provided by the USGS reports (http://earthquake.usgs.gov/earthquakes/eventpage/nc72282711#scientific_finitefault).

However, there are also some drawbacks that will require further investigations. Although California has one of the most dense GPS networks in the world, the main limitation comes from the limited number of GPS stations in close proximity of the epicentral area, where the largest co-seismic surface deformation occurred. This is the reason why the deformation pattern seems to be strongly led by the shape of the LOS displacement field detected by InSAR, although the values of the three position components are also influenced by the GPS measurements. In order to better constrain the N-S component, future developments regarding the data integration processing chain will be focused on the exploitation of other remote sensing techniques such as the Pixel Offset Tracking (POT).

The POT technique [Strozzi et al., 2002], based on pixel cross-correlation estimation, can measure displacements along the satellite azimuth direction, i.e. approximately N-S movements when considering quasi-polar orbits. Although it provides significant information for large deformation fields, however, the accuracy is not comparable with that of the InSAR and GPS measurements. The interpolation of the GPS displacements leads to errors affecting the quality of the estimates. Other interpolation techniques such as the Inverse Distance Weighting (IDW) will be explored in future developments by taking into account the spatial discontinuity due to the fault system.

Finally, as revealed by several studies [Barnhart et al., 2015; Brocher et al., 2015; Ji et al., 2015], the earthquake epicenter is located 1.7 Km westward of the known West Napa Fault system, and it mostly ruptured unmapped portions of this fault system. Therefore, to fully address all of the observed features, as well as to provide new insights about the slipping fault, additional investigations are required regarding, for example, the inversion of the optimized 3D co-seismic deformation field and the spatial and temporal distribution of the seismicity associated to the main shock.

## Acknowledgements

## References

Altamini Z., Metivier L., Collilieux X. (2012) - *ITRF2008 plate motion model*. Journal of Geophysical Research, 117 (B7). doi: http://dx.doi.org/10.1029/2011JB008930.

Barnhart W.D., Murray J.R., Yun S.-H., Svarc J.L., Samsonov S.V., Fielding E.J., Brooks B.A., Milillo P. (2015) - *Geodetic Constraints on the 2014 M 6.0 South Napa Earthquake*. Seismological Research Letters, 86: 335-343. doi: http://dx.doi.org/10.1785/0220140210.

Brocher T.M., Baltay A.S., Hardebeck J.L., Pollitz F.F., Murray J.R., Llenos A.L., Schwartz D.P., Blair J.L., Ponti D.J., Lienkaemper J.J., Langenheimb V.E., Dawsonc T.E., Hudnutd K.W., Shellye D.R., Dregerf D.S., Boatwrighta J., Aagaarda B.T., Waldg D.J., Allenf R.M., Barnharth W.D., Knudsena K.L., Brooksa B.A., Scharerd K.M. (2015) - *The M 6.0 24 August 2014 South Napa Earthquake*. Seismological Research Letters, 86 (2A): 309-326. doi: http://dx.doi.org/10.1785/0220150004.

Brooker P.I. (1991) - *A Geostatistical Primer*. World Scientific.

Costantini M. (1998) - *A novel phase unwrapping method based on network programming*. IEEE Transactions on Geoscience and Remote Sensing, 36 (3): 813-821. doi: http://dx.doi.org/10.1109/36.673674.

Fernández J., González P.J., Camacho A.G., Prieto J.F., Bru G. (2015) - *An Overview of Geodetic Volcano Research in the Canary Islands*. Pure and Applied Geophysics, 172 (11): 3189-3228. doi: http://dx.doi.org/10.1007/s00024-014-0916-6.

Goldstein R., Werner C. (1998) - *Radar interferogram filtering for geophysical applications*. Geophysical Research Letters, 25 (21): 4035-4038. doi: http://dx.doi.org/10.1029/1998GL900033.

González P.J., Tiampo K., Camacho A., Fernández J. (2010) - *Shallow flank deformation at Cumbre Vieja volcano (Canary Islands): Implications on the stability of steep-sided volcano flanks at oceanic islands*. Earth and Planetary Science Letters, 297: 545-557. doi: http://dx.doi.org/10.1016/j.epsl.2010.07.006.

Gudmunsson S., Sigmundsson F. (2002) - *Three-dimensional surface motion maps estimated from combined interferometric synthetic aperture radar and GPS data*. Journal of Geophysical Research, 107 (B10): ETG13-1-ETG13-14. doi: http://dx.doi.org/10.1029/2001JB000283.

Guglielmino F., Nunnari G., Puglisi G., Spata A. (2011) - *Simultaneous and Integrated Strain Tensor Estimation From Geodetic and Satellite Deformation Measurements to Obtain Three-Dimensional Displacement Maps*. IEEE Transactions on Geoscience and Remote Sensing, 49 (6): 1815-1826. doi: http://dx.doi.org/10.1109/TGRS.2010.2103078.

Hudnut K.W., Brocher T.M., Prentice C.S., Boatwright J., Brooks B.A., Aagaard B.T., Blair J.L., Fletcher J.B., Erdem J.E., Wicks C.W., Murray J.R., Pollitz F.F., Langbein J., Svarc J., Schwartz D.P., Ponti D.J., Hecker S., DeLong S., Rosa C., Jones B., Lamb

R., Anne M. Rosinski A.M., McCrink T.P., Dawson T.E., Seitz G., Rubin R.S., Glennie C., Hauser D., Ericksen T., Mardock D., Hoirup D.F., Bray J.D. (2014) - *Key recovery factors for the August 24, 2014, South Napa earthquake*. U.S. Geological Survey Open-File Report, 1249, p.51, doi: http://dx.doi.org/10.3133/ofr20141249.

Joyce K.E., Samsonov S.V., Levick S.R., Engelbrecht J., Belliss S. (2014) - *Mapping and monitoring geological hazards using optical, LiDAR, and synthetic aperture RADAR image data*. Natural Hazards, 73 (2): 137-163. doi: http://dx.doi.org/10.1007/s11069-014-1122-7.

Ji C., Archuleta R., Twardzik C. (2015) - *Rupture history of 2014 $M_w$ 6.0 South Napa earthquake inferred from near-fault strong motion data and its impact to the practice of ground strong motion prediction*. Geophysical Research Letters, 42 (7): 2149-2156. doi: http://dx.doi.org/10.1002/2015GL063335.

Li S. (2001) - *Markov random field modeling in image analysis*. Springer-Verlag. doi: http://dx.doi.org/10.1007/978-4-431-67044-5.

Malinverni E.S., Sandwell T.D., Tassetti A.N., Cappelletti L. (2014) - *InSAR decorrelation to assess and prevent volcanic risk*. European Journal of Remote Sensing, 47: 537-556. doi: http://dx.doi.org/10.5721/EuJRS20144730.

Palano M., Puglisi G., Gresta S. (2008) - *Ground deformation patterns at Mt. Etna from 1993 to 2000 from joint use of InSAR and GPS techniques*. Journal of Volcanology and Geothermal Research, 169: 99-120. doi: http://dx.doi.org/10.1016/j.jvolgeores.2007.08.014.

Polcari M., Albano M., Saroli M., Tolomei C., Lancia M., Moro M., Stramondo S. (2014) - *Subsidence detected by multi-pass Differential SAR Interferometry in the Cassino plain (Central Italy): joint effect of geological and anthropogenic factors?* Remote Sensing Journal, 6: 9676-9690. doi: http://dx.doi.org/10.3390/rs6109676.

Samsonov S., Tiampo K. (2006) - *Analytical Optimization of a DInSAR and GPS Dataset for Derivation of Three-Dimensional Surface Motion*. IEEE Geoscience and Remote Sensing Letters, 3 (1): 107-111. doi: http://dx.doi.org/10.1109/LGRS.2005.858483.

Samsonov S., Tiampo K., Rundle J., Li Z. (2007) - *Application of DInSAR-GPS Optimization for Derivation of Fine-Scale Surface Motion Maps of Southern California*. IEEE Transactions on Geoscience and Remote Sensing, 45 (2). doi: http://dx.doi.org/10.1109/TGRS.2006.887166.

Stramondo S., Bozzano F., Marra F., Wegmuller U., Cinti F.R., Moro M., Saroli M. (2008) - *Subsidence induced by urbanization in the city of Rome detected by advanced InSAR technique and geotechnical investigations*. Remote Sensing of Environment, 112: 3160-3172. doi: http://dx.doi.org/10.1016/j.rse.2008.03.008.

Strozzi T., Luckman A., Murray T., Wegmuller U., Werner C. (2002) - *Glacier motion estimation using SAR offset-tracking procedures*. IEEE Transactions on Geoscience and Remote Sensing, 40 (11): 2384-2391. doi: http://dx.doi.org/10.1109/TGRS.2002.805079.

Trasatti E., Polcari M., Bonafede M., Stramondo S. (2015) - *Geodetic constraints to the source mechanism of the 2011-2013 unrest at Campi Flegrei (Italy) caldera*. Geophysical Research Letters, 42: 3847-3854. doi: http://dx.doi.org/10.1002/2015GL063621.

Wegmuller U., Werner C. (1997) - *Gamma SAR processor and interferometry software*. In The 3rd ERS symposium on space at the service of our environment, Florence, Italy.

Wei S., Barbot S., Graves R., Lienkaemper J., Wang T., Hudnut K., Fu Y., Helmberger D.

(2015) - *The 2014 Mw 6.1 South Napa Earthquake: A Unilateral Rupture with Shallow Asperity and Rapid Afterslip*. Seismological Research Letters, 86 (2): 344-354. doi: http://dx.doi.org/10.1785/0220140249.